PAPER

Check for updates

Effect of Si substitution on the structural and transport properties of superionic Li-argyrodites†

Nicolò Minafra,[ac] Sean P. Culver,[a] Thorben Krauskopf,[a] Anatoliy Senyshyn[d] and Wolfgang G. Zeier [ID] *[ab]

Inspired by the recent interest in lithium ion conducting argyrodites as solid electrolytes for solid-state batteries, we have investigated the influence of aliovalent substitution in Li_6PS_5Br. Using Rietveld refinements against X-ray and neutron diffraction, coupled with impedance spectroscopy, we monitor the influence of Si^{4+} substitution for P^{5+} in $Li_{6+x}P_{1-x}Si_xS_5Br$ on the structure and ionic transport properties. A step-wise incorporation of Si^{4+} leads to an expansion of the unit cell, as well as the inclusion of additional Li^+ within the structure. The increasing Li content occupies the structural transition state and, in combination with the structural changes, leads to a three-fold improvement of the ionic conductivity. This work demonstrates that the argyrodite material class can be optimized through aliovalent substitution, thereby making argyrodites an ideal system for studying solid electrolytes within the field of solid-state batteries.

1. Introduction

Solid ion conductors (or solid electrolytes) have recently gained renewed interest due to their possible use in solid-state batteries. Using a fast Li^+ conducting solid provides the possibility to replace the ubiquitous liquid electrolytes, hopefully leading to safer and more reliable batteries.[1,2] Beyond oxide materials, such as garnets and the NASICON phosphates,[3–10] the class of thiophosphates shows great promise. Due to the more polarizable PS_4^{3-} anion, these soft materials exhibit high conductivities and low activation barriers, which are both important prerequisites for solid-state battery applications.[11–15] Despite the inherent instability of thiophosphates against Li metal anodes,[16–20] a multitude of materials are currently garnering a lot of attention, such as $Li_{10}GeP_2S_{12}$, Li_3PS_4, $Li_7P_3S_{11}$, thiophosphate glass ceramics and the argyrodites Li_6PS_5X.[14,21–39] However, a deeper understanding of the structural influence on the ionic conductivity is still missing for many materials.

[a]Institute of Physical Chemistry, Justus-Liebig-University Giessen, Heinrich-Buff-Ring 17, D-35392 Giessen, Germany. E-mail: wolfgang.g.zeier@phys.chemie.uni-giessen.de

[b]Center for Materials Research (LaMa), Justus-Liebig-University Giessen, Heinrich-Buff-Ring 16, D-35392 Giessen, Germany

[c]Dipartimento di Scienze Chimiche, Università Degli Studi di Padova, Via Marzolo 1, 35131, Padova, Italy

[d]Heinz Maier-Leibnitz Zentrum, Technische Universität München, 85748 Garching, Germany

† Electronic supplementary information (ESI) available: A scanning electron micrograph of an exemplary Li_6PS_5Br pellet and all tabulated structural data from Rietveld refinements against X-ray and neutron Bragg data. Further, all graphical results from the Rietveld refinements are shown. See DOI: 10.1039/c7ta08581h
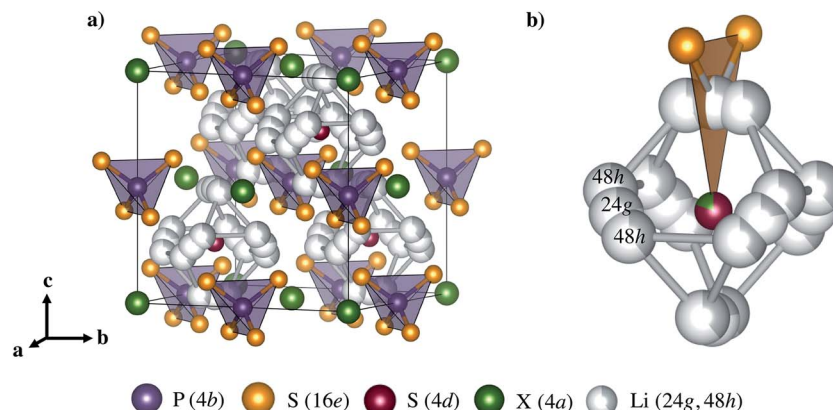
Fig. 1 shows the unit cell of Li_6PS_5Br. In a fully ordered structure, the Br^- anions form a face-centered cubic lattice ($4a$ Wyckoff position) with PS_4^{3-} polyhedra on the octahedral sites (P on Wyckoff $4b$) and S^{2-} anions in half of the tetrahedral voids on Wyckoff position $4d$ (sometimes denoted as $4c$, depending on the choice of origin and setting).[40] However, in the Br (and Cl) containing Li_6PS_5X argyrodites, a significant amount of site disorder between Br^- and S^{2-} has been found to exist and has been shown to influence the ionic transport.[26,36,41,42] Regarding the mobile ions, two Li^+ positions are known and are located on the $48h$ and $24g$ Wyckoff positions. Here, the $24g$ position acts as the transition state between jumps from $48h$–$48h$. In the composition Li_6PS_5Cl, the $48h$ position is occupied by exactly 50%, providing a vacant site on every next-neighbor position, which indeed makes these materials superionic.[43] However, Kraft *et al.*[14] recently found a lower occupancy for the $48h$ position in Li_6PS_5Br, with the residual Li^+ residing on the $24g$ transition state. Within the structure, the available Li^+ positions form cage-like local polyhedra for ion jumps that can be divided into three possible jump processes (see Fig. 1b), in which the site-disorder seems to positively affect the jump rate of Li^+ and may even alter the rate-determining jump.[14,36]

While many Cu^+ and Ag^+ containing argyrodites have been well studied from a structural point of view,[44–48] not much is known about the effect of aliovalent doping within the argyrodite class. Aliovalent doping in superionic compounds is often used in order to increase the number of charge carriers, and with it the ionic conductivity.[6,35,49–52] However, most argyrodite studies have so far focused on the isoelectronic substitution on the anion position,[14,26,33,36] leaving the question of the influence of more Li^+ in the structure unanswered. In order to better

This journal is © The Royal Society of Chemistry 2018

J. Mater. Chem. A, 2018, 6, 645–651 | 645

Fig. 1 (a) Crystal structure of Li_6PS_5Br. In the ordered structure, Br^- anions form a face-centered cubic lattice with the free S^{2-} in the tetrahedral sites and PS_4^{3-} in the octahedral voids. In Li_6PS_5Br, a site disorder between S^{2-} and Br^- is known as indicated in (b). (b) Li^+ positions forming polyhedral cages and a jump path that bypasses a transition state coordinated by the anions. Three different jump processes are possible such as the 48h–24g–48h jump, as well as 48h–48h jumps in the cage and between cages.

understand the effect of aliovalent doping in Li^+ conducting argyrodites, the substitution of P^{5+} with Si^{4+} was performed in the solid solutions $Li_{6+x}P_{1-x}Si_xS_5X$. By combining structural characterizations, *i.e.* X-ray and neutron diffraction with electrochemical impedance spectroscopy, we show the effect of increasing the Si^{4+} content on the ionic conductivity. While the larger Si^{4+} increases the size of the unit cell, it also increases the Li^+ concentration and leads to a rising occupancy of Li^+ on the transition state for hopping. This additional Si^{4+} increases the conductivity to greater than 2 mS cm^{-1}. This work shows the applicability of aliovalent doping in the superionic argyrodites, thereby demonstrating the optimization potential for this class of materials.

2. Experimental methods

Synthesis

All preparations and sample treatments for $Li_{6+x}P_{1-x}Si_xS_5X$ were carried out under argon atmosphere. Lithium sulfide (Li_2S, Sigma Aldrich, 99.98%), phosphorus pentasulfide (P_2S_5, Sigma Aldrich, 99%), as well as LiBr (ChemPur, 99.995%) and Si (ChemPur, 99%) were mixed in the appropriate stoichiometric ratio. All precursors were thoroughly dried using a vacuum oven before usage. All mixtures were hand ground in an agate mortar, pressed into pellets and then filled into quartz ampoules (10 mm inner diameter and 10–12 cm in length), which were sealed under vacuum. All ampoules were carbon-coated and pre-heated at 800 °C under dynamic vacuum to avoid all traces of water in the reaction atmosphere. The reactions were performed at 550 °C for two weeks in order to ensure a completeness of the reaction and phase purity. The obtained mixture was subsequently ground and isostatically pressed into pellets (10 mm diameter) for the electrochemical measurements or kept as powder for the diffraction studies.

X-ray diffraction

Structural investigations were carried out by means of X-ray powder diffraction using an Empyrean powder diffractometer

(PANalytical, Netherlands) with Cu Kα radiation ($\lambda_1 = 1.54051$ Å, $\lambda_2 = 1.54433$ Å) in Bragg–Brentano θ–θ geometry and a PIXcel3D area detector with 255 measuring channels. Samples were pulverized and placed on (911)-oriented silicon zero background holders that were sealed with Kapton foil under argon atmosphere. Patterns were collected in the range of 10–90° 2θ with a step size of 0.026° and an exposure time of 100 s per step.

Neutron powder diffraction

High-resolution neutron powder diffraction data collection on the argyrodite samples at room temperature was performed in a Debye–Scherrer geometry at the Heinz Maier-Leibnitz Zentrum (research reactor FRM II, Garching b. München, Germany) on the high-resolution diffractometer SPODI.[53] Data collection using one wavelength was performed, *i.e.* monochromatic neutrons ($\lambda = 1.54817(2)$ Å), and were obtained from the thermal neutron beam at a 155° take-off angle using the (551) reflection of a vertically focused composite Ge monochromator of 200 mm in height. The vertical position-sensitive multidetector (300 mm vertical sensitivity range at 1.117 m sample-to-detector distance) consisting of 80 ^{3}He tubes and covering an angular range of 160° 2θ was used for data collection. The samples (approx. 2 cm^3 in volume) were filled into thin-wall (0.15 mm) vanadium cans of 12 mm in diameter under an argon atmosphere and then metal-sealed using indium wire. The vanadium container was then mounted on a capillary spinner enabling sample rotation and thus, minimizing effects of preferred crystallite orientation. Two-dimensional powder diffraction data of the continuously rotated sample were collected and corrected for geometrical aberrations and detector nonlinearities.[54]

Rietveld analysis

Rietveld refinements were carried out using GSAS II software.[55] Fit indicators – R_{wp}, R_{exp}, and χ^2 – were used to assess the quality of the refined structural models.[56] The following parameters were initially refined: (1) scale factor, (2)

646 | *J. Mater. Chem. A*, 2018, **6**, 645–651

This journal is © The Royal Society of Chemistry 2018

background coefficients using a Chebyshev function with 30 parameters after a manual fitting, (3) peak shape, which was modeled using a modified Thomson–Cox–Hastings pseudo-Voigt function,[57] (4) lattice constants, (5) fractional atomic coordinates, and (6) isotropic atomic displacement parameters. The (7) atomic occupancies of the anions were then allowed to refine simultaneously with all other parameters, to quantify the anion site disorder, while the Si occupancy was fixed to the nominal content. Moreover, in the X-ray diffraction data the Li occupancies were fixed to the values extracted from the neutron refinement of Li_6PS_5Br and the isotropic atomic displacement parameters for Li were fixed to 0.05. Finally, (8) phase fractions and the associated lattice parameters of impurity phases were refined. The neutron refinements were conducted using the same procedure with several exceptions: (i) the background coefficients were fit using a Chebyschev function with 12 parameters and (ii) the Li occupancies and isotropic atomic displacement parameters were allowed to refine. (iii) Additional reflections of the vanadium sample holder can be found in the neutron diffraction patterns.

Electrochemical impedance spectroscopy

Electrical conductivities were measured by AC impedance spectroscopy, using pellets (1.5 mm thickness, geometric density of all samples ~85%) with vapor deposited gold layers. Electrochemical impedance analysis (EIS) was conducted in the temperature range of 20 °C to 60 °C using a SP300 impedance analyzer (Biologic) at frequencies from 7 MHz to 100 mHz with an amplitude of 10 mV. All measurements were performed in pouch cells under argon atmosphere.

Scanning electron microscopy

The microstructure of the electrolyte pellets was investigated using the Carl Zeiss Ultra field emission SEM instrument Merlin. The air sensitive samples were transferred from the glovebox to the vacuum chamber of the SEM with the Leica transfer module system EM VCT50. Additionally, a 5 nm Pt layer was sputtered onto the measured pellets.

3. Results and discussion

Structural characterization

The Li^+ superionic argyrodites $Li_{6+x}P_{1-x}Si_xS_5Br$ have been synthesized with increasing Si^{4+}/P^{5+} ratios in order to study the structural changes and the solubility limit of Si^{4+} in the structure, as well as to assess the effect of the increasing lithium content on the ionic conductivity. For the structural characterization, X-ray diffraction was performed on all samples. Moreover, due to the low X-ray form factor of Li^+, selected samples of ($x = 0$, 0.125 and 0.25) were also investigated using neutron diffraction to better probe the changing Li^+ substructure.

Fig. 2 shows a representative Rietveld refinement of an X-ray and a neutron diffraction pattern of $Li_{6.125}P_{0.875}Si_{0.125}S_5Br$. All samples exhibit minor impurity phase fractions of Li_3OBr and LiBr in the diffraction data for the series of solid solutions (see ESI†). The samples seem to react with the ampoules leading to an impurity phase fraction of ~2.8 wt% Li_3OBr in $Li_{6.125}P_{0.875}Si_{0.125}S_5Br$, despite the carbon coating and careful drying procedure of the silica ampoules. The minor impurities are unlikely to affect the ionic transport[14] and the obtained structural data of all solid solutions, obtained *via* Rietveld refinement against laboratory X-ray and neutron diffraction patterns, can be found tabulated in the ESI.†

Fig. 3 shows the structural data extracted from Rietveld refinements against the laboratory X-ray diffraction patterns. With increasing Si^{4+} content, the lattice parameter of the cubic structure increases linearly until it reaches a saturation level at 30 mol% ($x = 0.3$) of Si^{4+} content. The increasing lattice parameter arises from the larger ionic radius of Si^{4+} (26 pm, tetrahedrally coordinated) on the $4b$ tetrahedral site, compared to P^{5+} (17 pm, tetrahedrally coordinated).[58] This saturation suggests a solubility limit, after which a higher content of $x = 0.5$ does not lead to a further increase in the lattice parameter. With increasing x, an expanding MS_4 ($M = P_{1-x}Si_x$) polyhedral

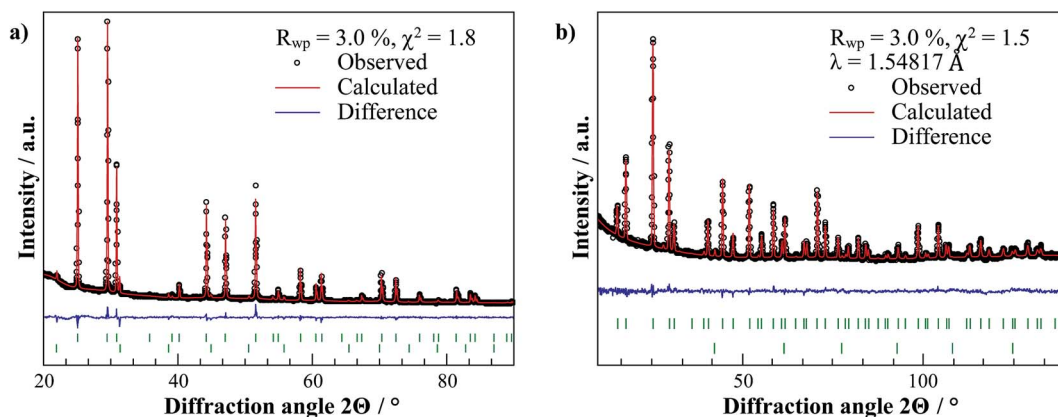**Fig. 2** (a) X-ray and (b) neutron powder diffraction data for $Li_{6.125}P_{0.875}Si_{0.125}S_5Br$ and the corresponding Rietveld refinements. Shown are the collected data, the profile fit, the profile residuals and the Bragg reflections for the main phase (top). A small fraction of the impurity phase Li_3OBr (bottom) can be seen in the X-ray diffraction pattern, which corresponds to ~2.8 wt%. Residual reflections in the neutron diffraction pattern stem from the vanadium sample holder (bottom Bragg reflections).

volume is observed, reflecting the larger radius of the substituting cation (see Fig. 3b). While a refinement of the Si^{4+}/P^{5+} fractional occupancies would unequivocally prove the site

substitution, Si^{4+} and P^{5+} are indistinguishable *via* X-rays and a stable refinement of the occupancies in the neutron diffraction data was not possible. However, the increasing polyhedral volumes and lattice parameters suggest successful incorporation of Si^{4+} on the P^{5+} site. It should be mentioned that Ge^{4+} substitution for P^{5+} in Li_6PS_5Br was also attempted; however, no lattice variations were observed, corroborating the negligible solubility of Ge in Li_6PS_5Br. As mentioned above, the Br^- anions should be crystallographically separated from the free S^{2-} anions, however a significant amount of site disorder is known due to the similar ionic radii of the Br^- and S^{2-} anions.[58] Fig. 3c shows the Br^-/S^{2-} site disorder found in the series of solid solutions, which does not appear to exhibit any major changes with the addition of Si^{4+}.

Fig. 4 shows the effect of the Si substitution on the Li^+ sub-lattice in $Li_{6+x}P_{1-x}Si_xS_5Br$, as obtained from the Rietveld refinement of the neutron diffraction patterns. With increasing nominal Si^{4+} content, the occupancy on the $24g$ Wyckoff position increases, while the occupancy of $48h$ position seems to remain constant (with a possible minor decline). It was recently shown that tailoring the anion framework in Li_6PS_5X by tuning the halide composition (*i.e.* from Cl to Br and finally to I), and increasing the unit cell dimensions, changes the lithium distribution over these two sites.[14] Here, a similar variation is
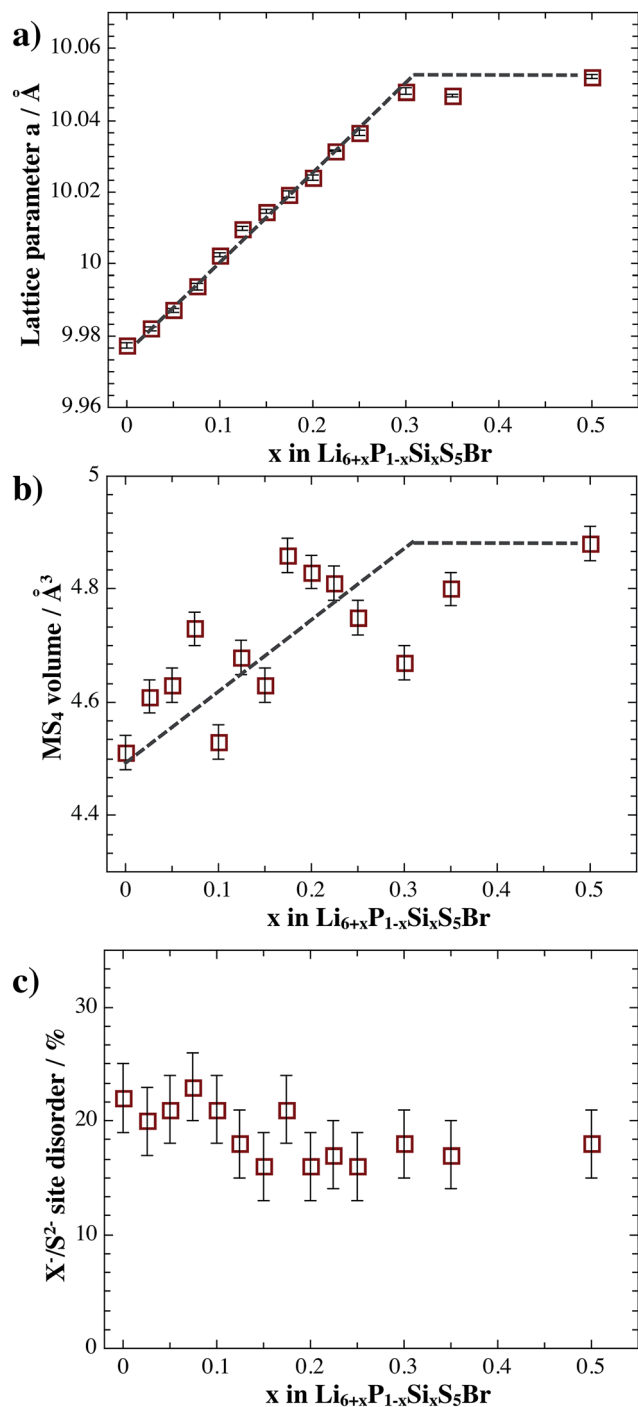

Fig. 3 Structural data of $Li_{6+x}P_{1-x}Si_xS_5Br$ obtained from the Rietveld refinements of X-ray diffraction patterns. (a) Increasing lattice parameters due to the larger ionic radius of Si^{4+}. At a composition of x = 0.3, a solubility limit is reached that is reflected by an upper limit in the lattice parameter. (b) Increasing MS_4 (M = $Si_{1-x}P_x$) polyhedral volumes due to the Si^{4+} substitution and resultant unit cell expansion. (c) Site disorder between Br^- and S^{2-}, which remains relatively constant with increasing x. The shown uncertainty reflects 3σ of the standard deviations obtained from the Rietveld refinement.
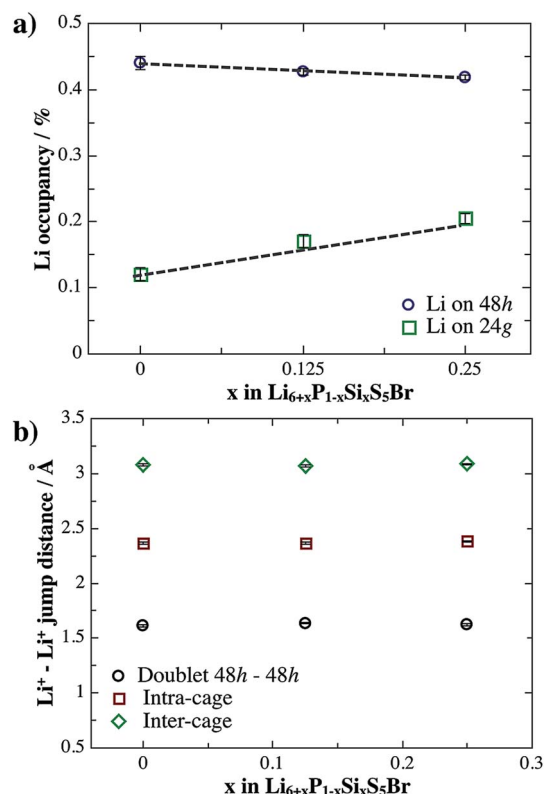

Fig. 4 Structural data of $Li_{6+x}P_{1-x}Si_xS_5Br$ obtained from the Rietveld refinements against neutron diffraction data. (a) Changing Li^+ occupancy on the two sites, in which an increasing Si^{4+} content leads to an increasing $24g$ occupancy. (b) Li^+–Li^+ jump distance that shows minor changes in the jump distances. The shown uncertainty reflects 3σ of the standard deviations obtained from the Rietveld refinement.

found in $Li_{6+x}P_{1−x}Si_xS_5Br$, where the inclusion of Si^{4+}, modification of the cation sublattice and the resultant unit cell expansion drives additional lithium cations to occupy the transition state of the jump process, *i.e.* Wyckoff 24*g*. Importantly, besides the lithium occupancy, the jump distances of the different Li^+ cations can further influence the diffusion as recently shown by Kraft *et al.*[14] While changing jump distances were found when altering the anion framework, Fig. 4b shows that the minor structural changes on the cation framework do not significantly affect the Li^+–Li^+ jump distances.

Ionic transport

Temperature-dependent impedance spectroscopy was performed on all samples to assess changes to the ionic conductivity. Arrhenius plots of representative samples ($x = 0$, 12.5, 25 and 50 are shown for clarity), and the corresponding impedance responses, are shown in Fig. 5a and b, respectively. An exemplary fit of the impedance data can be found in Fig. 5c. All impedance data were fit with an equivalent circuit consisting of one parallel CPE/resistor in series with a CPE, representing blocking electrodes. It should be noted that, due to the low reliability of high frequency data for such fast-ionic conductors, all fits were performed up to a maximum AC frequency of 1 MHz. All impedance spectra exhibit α-values of ∼0.9, representing the ideality of the CPE,[59] and geometric capacitances around 0.1 nF cm^{-2}. Additionally, while bulk and grain boundary contributions cannot be de-convoluted, the obtained ideality of the semi-circle and capacitances, as well as the high pellet densities (see scanning electron micrograph in the ESI†), correspond well with bulk transport.[60]

As seen in Fig. 5b, the impedance of the materials decreases with increasing Si^{4+} content, which corresponds to an increasing bulk conductivity. Accordingly, the room-temperature ionic conductivities of $Li_{6+x}P_{1−x}Si_xS_5Br$ are shown in Fig. 6a. With increasing Si^{4+} content, the amount of Li^+ increases and a three-fold increase in the conductivity from 0.7 mS cm^{-1} for the unsubstituted sample to 2.4 mS cm^{-1} for $Li_{6.35}P_{0.65}Si_{0.35}S_5Br$ can be observed. As the Si^{4+} content is increased further, the conductivity slightly decreases, possibly due to the solubility limit of Si^{4+} being surpassed and the associated phase segregations. However, the change in carrier density is very small, even for the 30 mol% Si^{4+} composition. Indeed, a 5% increase in the lithium concentration cannot account for a three-fold increase in the conductivity.

The Arrhenius data also provide information on the activation barrier for migration (Fig. 6b). Within the uncertainty in the investigated temperature range, no major changes to the activation energy E_A can be seen, even though a changing unit cell size and varying polyhedral volumes are known to affect the conductivity in ionic conductors.[10,14] Given that the here-seen changes in the polyhedral volumes are small, it may be possible that the changes in the conductivity may also be related to an additional underlying process. Notably, there are no significant variations in the site-disorder (see Fig. 3c) that would induce changes to the activation barrier.[14] One possible
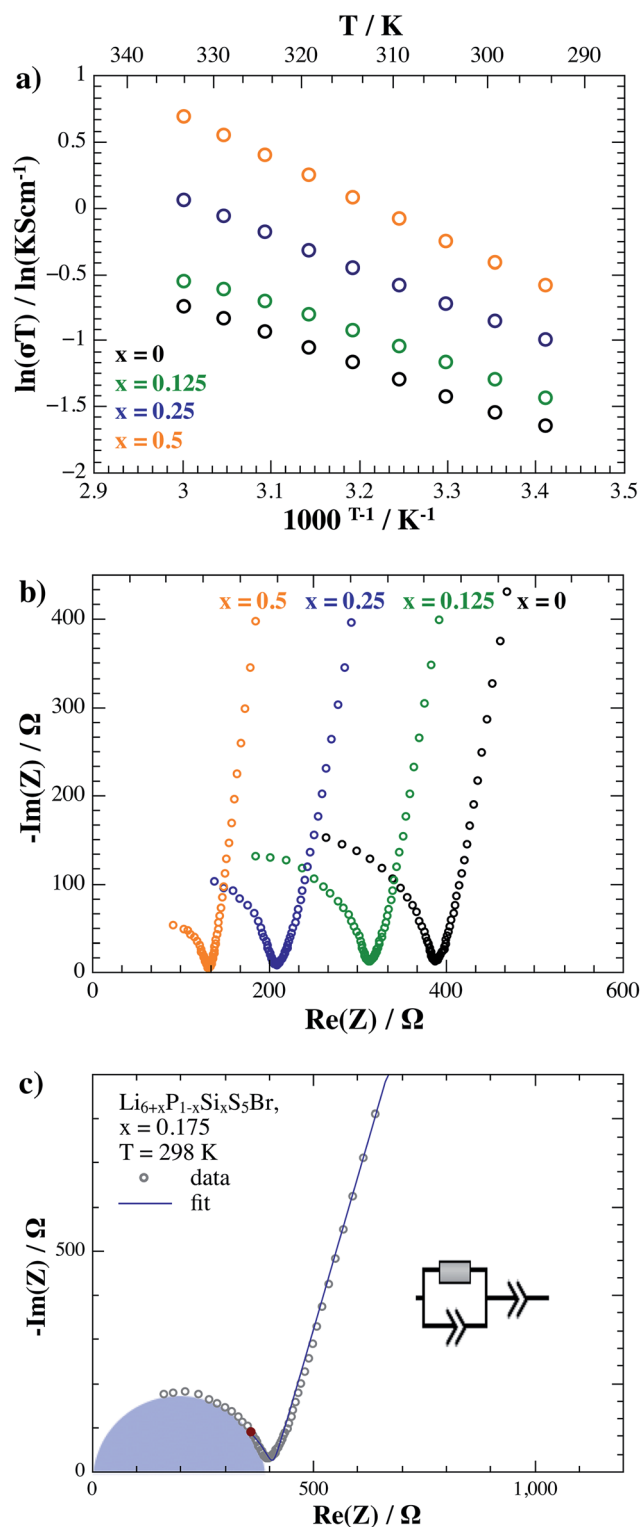

Fig. 5 (a) Representative Arrhenius fits of the conductivity values for $Li_{6+x}P_{1−x}Si_xS_5Br$ obtained from impedance spectroscopy and (b) the corresponding impedance responses at room temperature. (c) Representative fit of the composition $x = 0.175$ with the employed equivalent circuit. The data were fit until 1 MHz (red data point), providing a high ideality of the process and capacitances in the range of bulk transport (∼0.134 nF cm^{-2}). The apex frequency corresponds to 3.8 MHz.

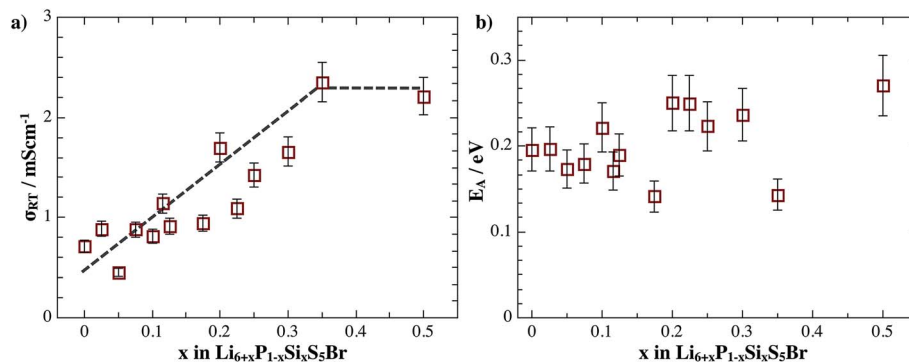This journal is © The Royal Society of Chemistry 2018

J. Mater. Chem. A, 2018, **6**, 645–651 | **649**

Fig. 6 (a) Room temperature conductivity of $Li_{6+x}P_{1-x}Si_xS_5Br$ as a function of Si^{4+} content. With increasing Si^{4+} content, the ionic conductivity increases, leading to the highest conductivity for $x = 0.35$. (b) Activation barrier E_A for ion migration, showing no visible dependence on the Si^{4+} content.

reason for the increase in the ionic conductivity may be enhanced Li^+–Li^+ correlation upon adding more Li^+ into the $24g$ site, as seen in the neutron diffraction data. The increasing population, and with it the coulombic repulsion, may lead to a correlated motion of ions, as opposed to single unrelated ion jumps. It has recently been shown that correlated motion of ions can beneficially affect the ionic conductivity by changing the Haven ratio, and with it the pre-factor, and even the activation barrier for hopping.[11] However, a combination of theoretical calculations, using *Ab Initio* Molecular Dynamics modelling, as well as Li^+ nuclear magnetic resonance experiments are necessary to confirm the existence of correlated motion in highly doped argyrodite superionics. Nevertheless, these data show that aliovalent substitution toward the optimization of the ionic conductivity in argyrodite superioncs is possible, though more theoretical work is necessary to fully understand the Li^+ motion and Li^+ interactions in this class of materials.

4. Conclusion

In this work, the effect of Si^{4+} substitution for P^{5+} in $Li_{6+x}P_{1-x}Si_xS_5Br$ has been investigated as a function of Si^{4+} content. Using a combination of X-ray diffraction, neutron diffraction and impedance spectroscopy, it is possible to probe the resultant structural changes and elucidate the structure–property relationships within Li-argyrodites when aliovalent substitutions are performed.

With increasing Si^{4+} substitution into the structure the lattice parameters increase up to a solubility limit and a threefold increase in the ionic conductivity can be observed. The structural data show that Si^{4+} incorporation increases the carrier concentration and polyhedral volumes, while adding more lithium cations into the transition state of hopping. Ultimately, the combination of a changing structure, elevated lithium content and enriched ion interactions lead to an increase in the conductivity, thereby corroborating that improvements to the ionic transport in the class of argyrodites are indeed possible.

Conflicts of interest

The authors declare no competing financial interests.

Acknowledgements

References

1 J. Janek and W. G. Zeier, *Nat. Energy*, 2016, **1**, 16141.
2 Y. Kato, S. Hori, T. Saito, K. Suzuki, M. Hirayama, A. Mitsui, M. Yonemura, H. Iba and R. Kanno, *Nat. Energy*, 2016, 16030.
3 B. E. Francisco, C. R. Stoldt and J.-C. M'Peko, *Chem. Mater.*, 2014, **26**, 4741–4749.
4 J. B. Goodenough, H.-P. Hong and J. A. Kafalas, *Mater. Res. Bull.*, 1976, **11**, 203–220.
5 M. Guin and F. Tietz, *J. Power Sources*, 2015, **273**, 1056–1064.
6 R. Murugan, V. Thangadurai and W. Weppner, *Ionics*, 2007, **13**, 195–203.
7 R. Murugan, V. Thangadurai and W. Weppner, *Angew. Chem., Int. Ed.*, 2007, **46**, 7778–8771.
8 V. Thangadurai and W. Weppner, *Adv. Funct. Mater.*, 2005, **15**, 107–112.
9 V. Thangadurai and W. Weppner, *Ionics*, 2006, **12**, 81–92.
10 W. G. Zeier, S. Zhou, B. Lopez-Bermudez, K. Page and B. C. Melot, *ACS Appl. Mater. Interfaces*, 2014, **6**, 10900–10907.
11 X. He, Y. Zhu and Y. Mo, *Nat. Commun.*, 2017, **8**, 15893.
12 Y. Wang, W. D. Richards, S. P. Ong, L. J. Miara, J. C. Kim, Y. Mo and G. Ceder, *Nat. Mater.*, 2015, **14**, 1026–1031.
13 J. C. Bachman, S. Muy, A. Grimaud, H. H. Chang, N. Pour, S. F. Lux, O. Paschos, F. Maglia, S. Lupart, P. Lamp, L. Giordano and Y. Shao-Horn, *Chem. Rev.*, 2016, **116**, 140–162.
14 M. Kraft, S. P. Culver, M. Calderon, F. Boecher, T. Krauskopf, A. Senyshyn, C. Dietrich, A. Zevalkink, J. Janek and W. G. Zeier, *J. Am. Chem. Soc.*, 2017, **139**, 10909–10918.

650 | *J. Mater. Chem. A*, 2018, **6**, 645–651

This journal is © The Royal Society of Chemistry 2018

15 T. Krauskopf, C. Pompe, M. Kraft and W. G. Zeier, *Chem. Mater.*, 2017, **29**, 8859–8869.

16 Y. Zhu, X. He and Y. Mo, *J. Mater. Chem. A*, 2016, **4**, 3253–3266.

17 Y. Zhu, X. He and Y. Mo, *ACS Appl. Mater. Interfaces*, 2015, **7**, 23685–23693.

18 S. Wenzel, S. Randau, T. Leichtweiß, D. A. Weber, J. Sann, W. G. Zeier and J. Janek, *Chem. Mater.*, 2016, **28**, 2400–2407.

19 S. Wenzel, T. Leichtweiss, D. A. Weber, J. Sann, W. G. Zeier and J. Janek, *ACS Appl. Mater. Interfaces*, 2016, **8**, 28216–28224.

20 W. D. Richards, L. J. Miara, Y. Wang, J. C. Kim and G. Ceder, *Chem. Mater.*, 2016, **28**, 266–273.

21 Z. Zhu, I.-H. Chu and S. P. Ong, *Chem. Mater.*, 2017, **29**, 2474–2484.

22 C. Yu, S. Ganapathy, N. J. J. de Klerk, I. Roslon, E. R. H. van Eck, A. P. M. Kentgens and M. Wagemaker, *J. Am. Chem. Soc.*, 2016, **138**, 1192–11201.

23 D. A. Weber, A. Senyshyn, K. S. Weldert, S. Wenzel, W. Zhang, R. Kaiser, S. Berendts, J. Janek and W. G. Zeier, *Chem. Mater.*, 2016, **28**, 5905–5915.

24 Y. Seino, T. Ota, K. Takada, A. Hayashi and M. Tatsumisago, *Energy Environ. Sci.*, 2014, **7**, 627–631.

25 Y. Seino, M. Nakagawa, M. Senga, H. Higuchi, K. Takada and T. Sasaki, *J. Mater. Chem. A*, 2015, **3**, 2756–2761.

26 P. R. Rayavarapu, N. Sharma, V. K. Peterson and S. Adams, *J. Solid State Electrochem.*, 2012, **16**, 1807–1813.

27 M. Murayama, R. Kanno, Y. Kawamoto and T. Kamiyama, *Solid State Ionics*, 2002, **154–155**, 789–794.

28 M. Murayama, R. Kanno, M. Irie, S. Ito, T. Hata, N. Sonoyama and Y. Kawamoto, *J. Solid State Chem.*, 2002, **168**, 140–148.

29 Y. Mo, S. P. Ong and G. Ceder, *Chem. Mater.*, 2012, **24**, 15–17.

30 C. Dietrich, D. A. Weber, S. J. Sedlmaier, S. Indris, S. P. Culver, D. Walter and W. G. Zeier, *J. Mater. Chem. A*, 2017, **5**, 18111–18119.

31 A. Kuhn, V. Duppel and B. V. Lotsch, *Energy Environ. Sci.*, 2013, **6**, 3548–3552.

32 A. Kuhn, J. Koehler and B. V. Lotsch, *Phys. Chem. Chem. Phys.*, 2013, **15**, 11620–11622.

33 S. T. Kong, O. Gün, B. Koch, H. J. Deiseroth, H. Eckert and C. Reiner, *Chem.–Eur. J.*, 2010, **16**, 5138–5147.

34 N. Kamaya, K. Homma, Y. Yamakawa, M. Hirayama, R. Kanno, M. Yonemura, T. Kamiyama, Y. Kato, S. Hama, K. Kawamoto and A. Mitsui, *Nat. Mater.*, 2011, **10**, 682–686.

35 S. Hori, K. Suzuki, M. Hirayama, Y. Kato, T. Saito, M. Yonemura and R. Kanno, *Faraday Discuss.*, 2014, **176**, 83–94.

36 N. J. J. de Klerk, I. Rosłoń and M. Wagemaker, *Chem. Mater.*, 2016, **28**, 7955–7963.

37 M. R. Busche, D. A. Weber, Y. Schneider, C. Dietrich, S. Wenzel, T. Leichtweiss, D. Schröder, W. Zhang, H. Weigand, D. Walter, S. J. Sedlmaier, D. Houtarde, L. F. Nazar and J. Janek, *Chem. Mater.*, 2016, **28**, 6152–6165.

38 P. Bron, S. Johansson, K. Zick, J. Schmedt auf der Günne, D. Günne, S. S. Dehnen and B. Roling, *J. Am. Chem. Soc.*, 2013, **135**, 15694–15697.

39 S. Adams and R. Prasada Rao, *J. Mater. Chem.*, 2012, **22**, 7687–7691.

40 S. T. Kong, H. J. Deiseroth, C. Reiner, O. Gün, E. Neumann, C. Ritter and D. Zahn, *Chem.–Eur. J.*, 2010, **6**, 2198–2206.

41 H. M. Chen, C. Maohua and S. Adams, *Phys. Chem. Chem. Phys.*, 2015, **17**, 16494–16506.

42 H. J. Deiseroth, S. T. Kong, H. Eckert, J. Vannahme, C. Reiner, T. Zaiß and M. Schlosser, *Angew. Chem., Int. Ed.*, 2008, **47**, 755–758.

43 Z. Wang and G. Shao, *J. Mater. Chem. A*, 2017, **5**, 21846–21857.

44 T. Zaiss and H.-J. Deiseroth, *Z. Kristallogr.–New Cryst. Struct.*, 2006, **221**, 119–120.

45 T. Nilges and A. Pfitzner, *Z. Kristallogr.*, 2005, **220**, 281–294.

46 E. Gaudin, H.-J. Deiseroth and T. Zaiss, *Z. Kristallogr.–Cryst. Mater.*, 2009, **216**, 39–44.

47 E. Gaudin, V. Petricek, F. Boucher, F. Taulelle and M. Evain, *Acta Crystallogr., Sect. B: Struct. Sci.*, 2000, **56**, 972–979.

48 E. I. Gaudin, H. J. Deiseroth and T. Z. Ii, *Z. Kristallogr.*, 2001, **216**, 39–44.

49 J. B. Goodenough, *Solid State Ionics*, 1997, **94**, 17–25.

50 O. Kwon, M. Hirayama, K. Suzuki, Y. Kato, T. Saito, M. Yonemura, T. Kamiyama and R. Kanno, *J. Mater. Chem. A*, 2015, **3**, 438–446.

51 M. P. O'Callaghan and E. J. Cussen, *Chem. Commun.*, 2007, **12**, 2048–2050.

52 M. P. O'Callaghan, A. S. Powell, J. J. Titman, G. Z. Chen and E. J. Cussen, *Chem. Mater.*, 2008, **20**, 2360–2369.

53 M. Hoelzel, A. Senyshyn and O. Dolotko, *Journal of large-scale research facilities*, 2015, **1**, 5.

54 M. Hoelzel, A. Senyshyn, N. Juenke, H. Boysen, W. Schmahl and H. Fuess, *Nucl. Instrum. Methods Phys. Res., Sect. A*, 2012, **667**, 32–37.

55 B. H. Toby and R. B. Von Dreele, *J. Appl. Crystallogr.*, 2013, **46**, 544–549.

56 R. A. Young, *The Rietveld Method*, Oxford University Press, New York, 1993.

57 P. Thompson, D. E. Cox and J. B. Hastings, *J. Appl. Crystallogr.*, 1987, **20**, 79–83.

58 R. D. Shannon, *Acta Crystallogr., Sect. A: Cryst. Phys., Diffr., Theor. Gen. Crystallogr.*, 1976, **32**, 751–767.

59 G. J. Brug, A. L. G. van den Eeden, M. Sluyters-Rehbach and J. H. Sluyters, *J. Electroanal. Chem.*, 1984, **176**, 275–295.

60 J. T. S. Irvine, D. C. Sinclair and A. R. West, *Adv. Mater.*, 1990, **2**, 132–138.

This journal is © The Royal Society of Chemistry 2018

J. Mater. Chem. A, 2018, **6**, 645–651 | **651**